Deep Resources Engineering 2 (2025) 100166

Contents lists available at ScienceDirect

Deep Resources Engineering

journal homepage: www.keaipublishing.com/en/journals/deepre/

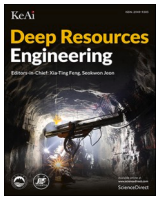

Full Length Article

Partly clumped-particles for elastic mismatch of minerals and joint planes for schist: A numerical simulation of DanBa quartz mica schist

Xiao-Ping Zhang [a,*], Shunchuan Wu [b,c], Sijing Wang [d]

[a] The Key Laboratory of Safety for Geotechnical and Structural Engineering of Hubei Province, School of Civil Engineering, Wuhan University, Wuhan 430072, China
[b] Faculty of Land Resources Engineering, Kunming University of Science and Technology, Kunming, Yunnan 650093, China
[c] School of Civil and Resource Engineering, University of Science and Technology Beijing, Beijing 100083, China
[d] Institute of Geology and Geophysics, Chinese Academy of Sciences, Beijing 100029, China

ARTICLE INFO

Keywords:
Elastic mismatch
Schist
Particle element simulation
Uniaxial compressive test

ABSTRACT

A partly clumped-particles combined with joint planes model was developed to simulate the microstructure of quartz mica schist. It considers grain-scale heterogeneity including microgeometry heterogeneity and grain-scale elastic heterogeneity. Clumped-particles with larger volume and larger stiffness were used to represent stiff minerals such as quartz, the rest of unclumped particles with smaller stiffness were used to represent soft minerals such as mica. The joint planes, which have smaller stiffness and strength than mica, were used to describe schist. The extensive sensitivity studies have shown that the clump's radius, clump's content and joint plane's strength affect the microscopic and macroscopic behaviors of sample. For DanBa quartz mica schist, the model calibrated uniaxial tests and well matched with the stress-strain curves, crack initiation stress and crack damage stress of laboratory test.

1. Introduction

Rock, being a heterogeneous material in nature, can be characterized by its internal microstructure. Quartz mica schist contains quartz and mica as its essential components. Quartz is harder than mica, so a heterogeneous caused by elastic mismatch exists. Arup K. Khaund[1] has reported elastic mismatch influences the crack path as well as crack velocity in brittle composites. Kee Sung Lee [2] has found that the larger the elastic mismatch between the coating and the substrate laygers is, the lower the loading of initiation of cracks occurred at during the contact. P. D. Warren [3] has demonstrated that in brittle materials, the progression of surface flaws into cracks is significantly hindered when the indenter is stiffer than the substrate, and conversely, when the substrate is stiffer than the indenter, the development is less impeded. Rock is a heterogeneous material which has elastic mismatch phenomena, while quartz mica schist is such a typical rock. Despite elastic mismatch, quartz mica schist is a transverse anisotropy material with fabric which is symmetrical about an axis perpendicular to the foliation [4].

In the present study, in order to obtain the micro cracking and anisotropic characteristics of quartz mica schist, the partly clumped-particles with Joint planes model have been examined based on bonded particle model. In the mixture of quartz and mica (stand for hard and soft minerals respectively), quartz have larger elastic modulus than mica (Table 1). The mechanism behind the formation of compression-induced tensile cracks is illustrated in Fig. 1. Under the same stress, the harder component (depicted in light gray) undergoes less deformation compared to the softer part (in white), leading to tensile stress in the restraining bond. Besides the initiation and propagation of microcracks, their eventual interaction is crucial for triggering localization phenomena, such as axial splitting or the formation of rupture zones, during unconfined or confined compression tests.

2. Partly clumped-particle model for quartz mica mixture

2.1. Partly clumped-particle

The bonded particle model (referred to hereafter as the BPM) which describes the rock behaves like a cemented granular material has received considerable attention for its ability to simulate non-linear behaviors and progressive failure process of rock. The BPM necessitates neither any flow rule to delineate the post-yield response nor fracture toughness to govern fracture behavior; it solely relies on the principles governing particle deformation and the criteria for particle bond rupture. Potoyondy and Cundall [8] , A.Fakhimi [9] and N. Cho, C.D. Martin,et,

* Corresponding author.
E-mail addresses: jxhkzhang@163.com (X.-P. Zhang), wushunchuan@ustb.edu.cn (S. Wu).

https://doi.org/10.1016/j.deepre.2025.100166
Received 7 December 2024; Received in revised form 11 February 2025; Accepted 11 February 2025
Available online 14 February 2025

Table 1
Moduli of common minerals in quartz mica schist.

	Quartz	Muscovite	Biotite	Plagioclase	"average"feldspar
Elastic modulus/ Gpa	95.76	77.37	33.80	69.01	39.71
Poisson's ratio	0.06	0.25	0.36	0.35	0.32
References	[5]	[6]	[7]	[8]	[9]

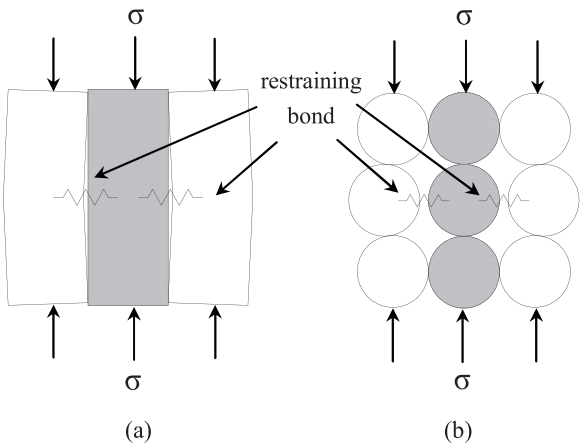

Fig. 1. Physical mechanisms for elastic mismatch between grains compression-induced tensile cracking (a) and idealization as bonded assembly of circular particles (b) White color stands for soften material, light gray stands for hard material.

al.[10] have paved the way of BPM to simulate rock material.

Besides the macro-mechanical simulation of rock, BPM has much more merits on the description of formation, growth and eventual interaction of micro-cracks, which govern the macro-mechanical behavior of rock. Experimental observations have shown that compression-induced cracks predominantly align parallel to the direction of maximum compression. Kemeny and Cook [11] underscore the significance of generating such compression-induced tensile cracks, highlighting that laboratory tests on rocks undergoing differential compression have unveiled a multitude of mechanisms responsible for extensile crack propagation. These mechanisms include pore crushing, sliding along pre-existing fractures, elastic mismatch among grains, dislocation movement, and Hertzian contact. Here we mainly discuss cracks induced by elastic mismatch between grains as well as sliding along pre-existing schist of mica.

Several studies have demonstrated that grain size and specific surface area are crucial parameters for elucidating the variations in mechanical properties among rock types of identical composition [12]. Lundquist and Goransson proposed that the shape of mineral grains, the distribution of grain sizes, and the quantity of fine-grained matrix play significant roles in determining the mechanical properties of rocks [13]. However, it is equally important to distinguish boundaries between minerals of the same phase (such as quartz-quartz) from those between minerals of different phases (like quartz-biotite). The latter represents a boundary separating materials with distinct atomic lattices, bond types, strengths, and moduli of elasticity (E-modulus), which can lead to varied modes of microfracture propagation [14]. Hengxing Lan [15] developed a grain-based Universal Distinct Element Code model to create a deformable polygonal grain-like structure, mimicking the microstructure of brittle rocks. Their findings indicate that the crack-initiation stress is primarily governed by microscale geometric heterogeneity, whereas the strength characteristics are controlled by microcontact heterogeneity. In this part, partly clumped-particle model is adopted to simulate the different phases of quartz-mica mixture.

In PFC2D, the clump logic offers a methodology for creating and modifying groups of particles, known as clumps, that behave as a rigid body. During the calculation cycle, the particles within a clump maintain a fixed distance from each other. Contacts with particles external to the clump remain unaffected and develop only when the particles constituting the boundary of the clump encounter other particles [16]. Through clump logic, clumped-particles have larger stiffness were used to represent stiff minerals such as quartz, the rest of unclumped particles have smaller stiffness were used to represent soft minerals such as mica. The main reason for such a consideration is the crystal shape, as shown in Fig. 2, quartz has nearly the same size in width and in length, while mica have much larger size in length than in width, and the width of mica are several times shorter than the width of quartz, a clump contains several particles near each other, and each clump is grown by identifying the current particles as a seed particle and then adding adjacent particles to the clump until the clump size has reached assigned value, so a clump which is actually a large particle with irregular boundary can describe quartz, the rest unclumped particles were divided by joint planes to describe mica. We use this partly clumped-particles assemble to represent quartz mica mixture.

As a matter of fact, a clump will not break up under stress for it behaves as a rigid body. Clumps are used to represent stiff minerals assuming that stiff minerals harder enough than soft minerals and will not break up, micro cracking just occurs between unclumped particles or between the clump and unclumped particles interface.

As shown in Fig. 2, we did not intend to strictly match the grain size and grain distribution to actual grains in terms of similarity, the random model used to make the contents of clumped-particles equals to the contents of quartz in the photomicrograph.

2.2. *Effect of micro-parameters in BPM*

The bonded-particle model code utilized in the present study was PFC2D, developed by the ITASCA Consulting Group for commercial purposes. Since its initial release in 1995, PFC2D has been extensively used in numerous research projects. PFC2D represents a rock mass as an assembly of circular disks with finite thickness (or spheres with a single layer in the out-of-plane direction) that are connected through cohesive and frictional bonds, featuring finite stiffness at the contact and bonded areas between disks. When the local stresses (such as tension, shear, or moment due to particle rotation) exceed the specified bond strengths, these bonds break, leading to the formation of a rupture surface, or crack. Notably, PFC does not necessitate any flow rule to describe the post-yield response or fracture toughness to control fracture behavior during these processes. Instead, it solely relies on the law of motion for particle movement, simple constitutive laws for particle deformation, and yielding laws for particle bond rupture. There are many more detailed introductions in literatures [8,10, 16]. Parallel Bond model is one of the basic bond models provided in PFC, which approximates the physical behavior of a cement-like substance joining the two adjacent particles. The main microparameters that characterize a parallel-bonded material are given below:

$$\{R_{\min}, R_{\max}/R_{\min}, \rho, E_c, (k_n/k_s), \mu\}, \quad \text{particlemicroproperties}, (\text{describegrain})$$

$$\{\bar{\lambda}, \bar{E}_c, (\bar{k}^n/\bar{k}^s), \bar{\sigma}_c, \bar{\tau}_c\}, \quad \text{parallelbondmicroproperties}, (\text{describecement}) \tag{1}$$

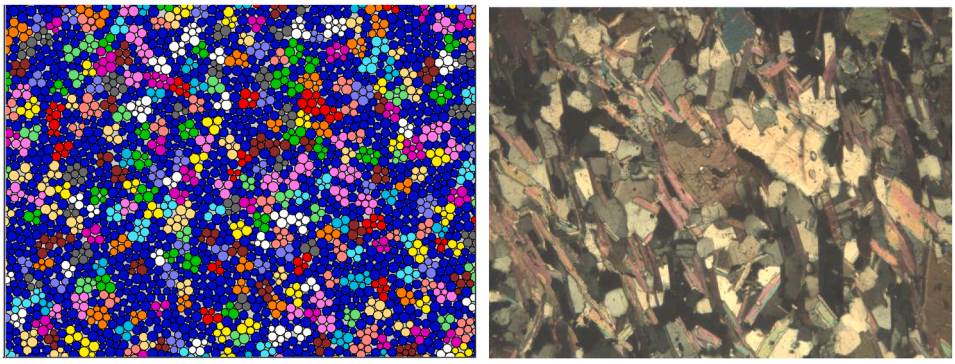

partly clumped-particles photomicrograph of quartz mica schist(2.61×1.96mm)

Fig. 2. Partly clumped-particles for quartz mica mixtures, the blue particles are unclumped particles stands for mica, the others are clumped particles for quartz, the same color particles near each other form a clump.(haven't induced joint planes for schist yet).

Where

R_{min} and R_{max}/R_{min} describe the particle diameters, which satisfy a uniform particle size distribution bounded by R_{min} and R_{max};

ρ is the particle density;

E_c and $\overline{E}_c$ are the Young's moduli of the particle and parallel bond, respectively;

(k_n/k_s) and $(\overline{k}^n/\overline{k}^s)$ are the ratios of normal to shear stiffness of the particles and parallel bond, respectively;

$\overline{\lambda}$ is the radius multiplier used to set the parallel-bond radius $\overline{R}$ via:

$$\overline{R} = \overline{\lambda}\min\left(R^{(A)}, R^{(B)}\right), \quad R \text{ isparticleradius} \tag{2}$$

μ is the grain friction coefficient;

$\overline{\sigma}_c$ and $\overline{\tau}_c$ are the tensile and shear strengths, respectively, of the parallel bond.

In the subsequent analysis, the moduli of the grain and cement are correlated with their respective normal stiffnesses, with the particle and parallel bond stiffnesses being assigned accordingly. $k_n = 2tE_c, t = 1$, $k_s = \frac{k_n}{k_n/k_s}$,

$$\overline{k}^n = \frac{\overline{E}_c}{R^{(A)} + R^{(B)}}, \overline{k}^s = \frac{\overline{k}^n}{(\overline{k}^n/\overline{k}^s)}, \tag{3}$$

To determine the normal stiffnesses, we envision the material at each contact as an elastic beam with its ends located at the particle centers, as illustrated in Fig. 3. It has been demonstrated that the macroscopic elastic constants in PFC2D are independent of particle size [8].

Relative motion at the parallel-bonded contact results in the development of axial and shear directed forces (T and V, respectively) as well as a moment (M). The maximum normal and shear stresses ($\overline{\sigma}$and$\overline{\tau}$, respectively) carried by the bonding material can be expressed as:

$$\overline{\sigma} = \frac{T}{A} + \frac{|M|\overline{R}}{I}, A = 2\overline{R}t, I = \frac{1}{12}t(2\overline{R})^3$$
$$\overline{\tau} = \frac{|V|}{A} \tag{4}$$

Where A and I represents the area and moment of inertia of the parallel-bond cross-section respectively (Fig. 3(b)), and positive T indicates tension. When either $\overline{\sigma}$or $\overline{\tau}$exceeds the corresponding strengths ($\overline{\sigma}_c$,$\overline{\tau}_c$), the bond breaks, forming a tension crack or shear crack between two particles.

The PFC micro-parameters were analyzed through simulations of both uniaxial compressive tests and Brazilian tests. During the uniaxial test simulation, the lateral strain, axial strain, and peak strength were documented. Meanwhile, the tensile strength was determined using the Brazilian test simulation. The methods for generating samples and applying loads were detailed in references [8,16]. Due to the inherent heterogeneity in PFC, such as the application of a standard deviation to micro-strength and the arbitrary generation of disk assemblies with varying particle radii, no two PFC runs will yield identical results [10]. In this parametric study, each simulation was conducted ten times using the same parameters, and the results were averaged to approximate the variability observed in rock testing. Although this approach is somewhat time-consuming, it helps to avoid obtaining unique, potentially irrelevant answers and provides a more realistic representation of the variability encountered in rock testing [10].

The PFC specimens for uniaxial compressive test were measured 50 mm× 100 mm and consisted of 3732 particles. The tests are conducted under displacement control, where the platens move towards one another at a constant speed. The loading rate was set sufficiently slow to ensure that the sample remained in quasi-static equilibrium throughout the test, maintaining stability and preventing any potential strength

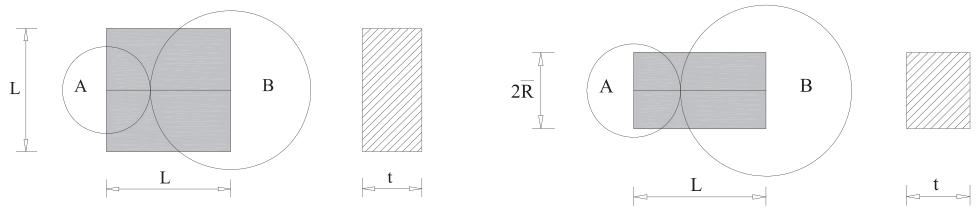

(a) particle-particle contact (b) parallel-bonded contact

$$E_c = \frac{k_n}{2t}, \quad t = 1 \qquad \overline{E}_c = \overline{k}^n(R^{(A)} + R^{(B)})$$

Fig. 3. Equivalent continuum material of parallel-bonded particles system.

increase or unexpected material responses within the simulated models [17–21].

2.2.1. Effect of Young's modulus

In BPM, there are two parts of Young's modulus at each parallel-bonded contact: $E_c$is the Young's modulus at each particle to particle contact, $\overline{E}_c$ is the Young's modulus of each parallel bond. The overall modulus at a parallel-bonded contact (at which the two bonded particles have a nonzero overlap) is the sum of E_c and$\overline{E}_c$. When a parallel bond breaks, the overall modulus at the contact is reduced by$\overline{E}_c$, which also correct for rock materials after microcrack be produced. The problem is how to divide these two parts; many special experiments may need to get the modulus reduction of broken mineral. For this reason, no attempt was made for dividing the modulus and only to be fixed to 50 % of each part.

Young's modulus between two particles different from particles assembly, the latter always lower than the former. we assign particle's Young's modulus according to Table 1, take Biotite as an example, the micro parameters of Biotite is shown in Table 2, the calculated Young's modulus of particles assembly is 20Gpa, which is lower than 33.8Gpa (the sum of E_c and $\overline{E}_c$). It is true that rock's Young's modulus is lower than mineral's. In this model for quartz and mica mixture, the mineral's Young's modulus for micro-cracking analysis is mainly taken into account other than rock's Young's modulu.

2.2.2. Effect of Poisson's ratio

Besides Young's modulus, Poisson's ratio is another important measure to describe material's deformation characteristic. As is mentioned before, from the uniaxial test simulation, lateral and axial strain could be recorded; Poisson's ratio is given by the ratio of lateral strain to axial strain. In PFC model, Diederich [22] and Potyondy and Cundall [8] were shown that the stiffness ratio (normal to shear ratio for both contact and bond) directly involves Poisson's ratio. As the stiffness ratio increases (the rest parameters are shown in Table 2), Poisson's ratio also increases and the sample becomes ductile (Fig. 4). Both contact and bond stiffness ratio were varied from 1.0 to 10.0. Fig. 4 indicates that as stiffness ratio is increased, the amount of the ratio of tension crack numbers to total crack numbers also increases, when stiffness ratio reaches 4.5 or larger, more than 90 % cracks are in the form of tension crack.

However, it is important to note that direct comparison of Poisson's ratio in PFC2D with laboratory results may not be meaningful due to the limitations of 2D analysis in PFC [8,10]. The fundamental assumption in PFC2D for particle elements is that particles are either disks with finite thickness or spheres with a single layer in the out-of-plane direction. While the former resembles the plane strain condition and the latter resembles the plane stress condition in continuum mechanics, PFC2D differs from continuum mechanics assumptions in that there is no out-of-plane stress in plane strain and no out-of-plane strain in plane stress. Therefore, attempts to match volumetric strain or Poisson's ratio in PFC2D material to 3D physical material may not always be successful.

2.3. Partly clumped-particle model for elastic mismatch of minerals

2.3.1. Partly clumped-particle model

A clump exhibits rigid body behavior, with its constituent particles

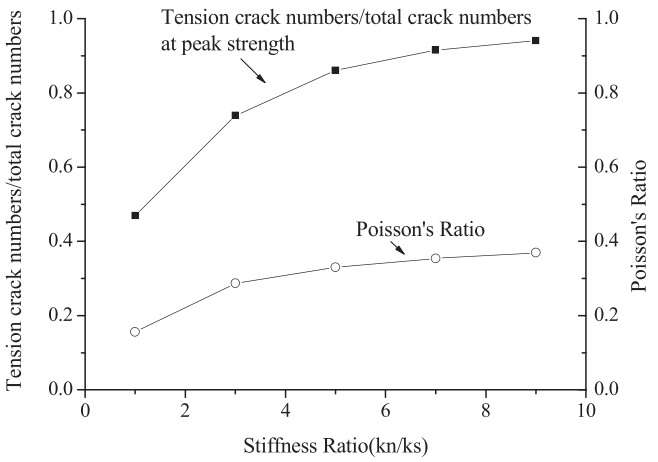

Fig. 4. Effect of contact and bond stiffness ratio on Poisson's ratio and tension crack numbers to total crack numbers at peak strength.

maintaining a constant distance from each other throughout the calculation cycle. Contacts with particles outside the clump remain unaffected, and these external contacts arise when particles forming the boundary of the clump encounter other particles. So clumped particles can act like a single particle that has an irregular shape but move as a rigid body. A partly clumped-particle assemble is the mixture of circular particles and large particles with irregular shape.

In a totally clumped particle model N. Cho and C.D. Martin[10] were shown that clump size(clp_rad), bond normal strength(σ_n) and ratio of shear strength to normal strength ($\overline{\sigma}_s/\overline{\sigma}_n$) were the parameters which could affect both uniaxial strength and slope of failure envelope. In this section, clump's radius, clump's content and the accumulations of crack in partly clumped-particle model were tested. The micro-parameters for quartz mica schist used in this analysis are given in Table 2(for biotite) and Table 3(for quartz). The trial-and-error method was employed based on the effect study outlined in Section 2.2 and relevant references [8,16, 23], to minimize the number of attempts. The calibration factors, which encompass the parameter range, primarily involve fixing the strength parameters in a certain range initially to facilitate the study of clump and joint planes parameters. Since biotite is a mineral with relatively low strength within a certain range, the parallel bond strength values ($\overline{\sigma}_c$and$\overline{\tau}_c$) for biotite have been fixed at ± 8 MPa (see Table 2). In contrast, for the strong mineral quartz, we assume that the parallel bond strength values ($\overline{\sigma}_c$and$\overline{\tau}_c$) remain constant at ± 0 MPa (see Table 3).

2.3.2. Effect of clump's radius

N. Cho and C.D. Martin [10] suggested that as clump size increases, dilation is significantly increased but the ratio of tensile to uniaxial compression strength σ_t/σ_{ci} is reduced. In partly clumped-particle model, the ratio of clumped-particle volume to unclumped-particle volume was kept as a constant of 1.5 in the following calculation, the clump's radius was made as a variable in order to get different outcomes. Unlike totally clumped particle model concern dilation and the strength ratio σ_t/σ_{ci}[10], this research will focus on Elastic modulus, crack initiation stress and peak strength for the elastic mismatch as well as stress concentration caused by partly clumped particles.

Table 2
The micro parameters of biotite.

E_c	16.9Gpa	$\overline{E}_c$	16.9Gpa
k_n/k_s	2.5	$\overline{k}_n/\overline{k}_s$	2.5
μ	0.1	$\overline{\sigma}_c$	30Mpa± 8Mpa
R_{max}/R_{min}	1.66	$\overline{\tau}_c$	30Mpa± 8Mpa
R_{min}	0.45 mm	$\overline{\lambda}$	1.0
ρ	3210 kg/m^3		

Table 3
The micro parameters of quartz.

E_c	47.88Gpa	$\overline{E}_c$	47.88Gpa
k_n/k_s	0.6	$\overline{k}_n/\overline{k}_s$	0.6
μ	0.1	$\overline{\sigma}_c$	60Mpa ± 0Mpa
R_{max}/R_{min}	1.66	$\overline{\tau}_c$	60Mpa ± 0Mpa
R_{min}	0.45 mm	$\overline{\lambda}$	1.0
ρ	3210 kg/m^3		

Martin and Chandler [24] described a typical procedure to determine the crack-initiation stress from laboratory testing results. In conventional laboratory tests, the crack-initiation stress is defined as the stress at which dilation first appears on a plot of crack volumetric strain. These strains are calculated from the total volumetric strains [25,26]. While this method is effective for obtaining crack initiation stress from laboratory tests, it is not suitable for PFC2D materials. As previously demonstrated, the volumetric response and Poisson's ratio of two-dimensional PFC2D materials cannot be directly compared to those of three-dimensional physical materials [10].

Potyondy and Cundall [8] proposed that the crack initiation stress can be estimated by considering the stress magnitude that corresponds to 1–2 % of the total number of cracks at the peak stress during the biaxial simulation of PFC synthetic rock. In the present study, the crack initiation stress corresponds to approximately 2 % of total number of cracks were taken into consideration.

The results were given in Fig. 5 shown clearly that as clump size increases, elastic modulus is significantly increased. While the peak strength was reduced from 53.3Mpa to 38.8Mpa for clump radius increased from 1.5 mm to 8 mm. The crack initiation stress was also reduced for clump radius increases from 3 mm to 7 mm. It is worth noting that if the average clump radius was too small (close to the particle size) or too large (close to the specimen size), the trend may reversed slightly and revealed fluctuate.

Except for the extremity clump radius (too small or too large), the larger the clump size is, the more intensity stress concentration (Fig. 6) near some clumps would be, while the stress exceeds bond strength of particle-particle or particle-clump, then breaks occur. So initiation stress of large clump size conditions are lower than small size, and the peak strength of large clump size conditions are lower accordingly.

2.3.3. *Effect of clump's content in assemble*

The clump acts as a single rigid body which contains a group of glued particles, these particles have larger Elastic modulus and bond strength than unclumped particles (see Table 2 for biotite, Table 3 for quartz), so contacts with particles external to the clump are stiffer and stronger than unclumped particles.

In addition, N. Cho and C.D. Martin [10] suggested that excessive particle rotation was restricted by taking the clump logic (Fig. 7). Fig. 8 clearly demonstrates that when particle rotation is completely suppressed, the peak strength increases significantly (by an order of magnitude). However, it is impractical to suppress all rotation since force chains clearly indicate that bending does occur. While clumped particles can mitigate the impact of particle rotation, they still allow for proper simulation of moment loading.

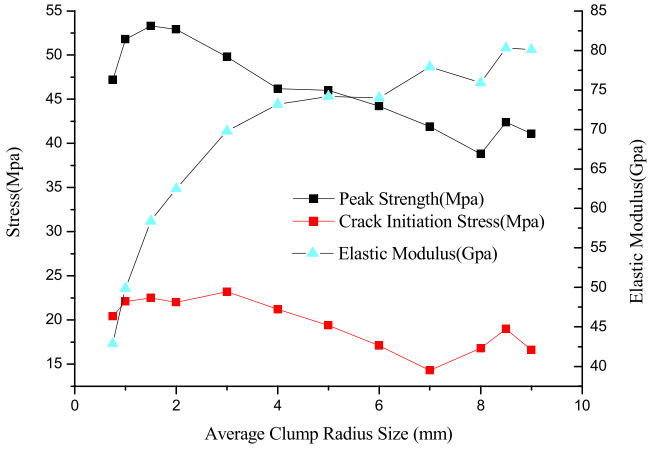

Fig. 5. Effect of the clump radius on peak strength and crack initiation stress as well as elastic modulus (The ratio of clumped-particle volume to unclumped-particle volume was kept 1.5 for all).

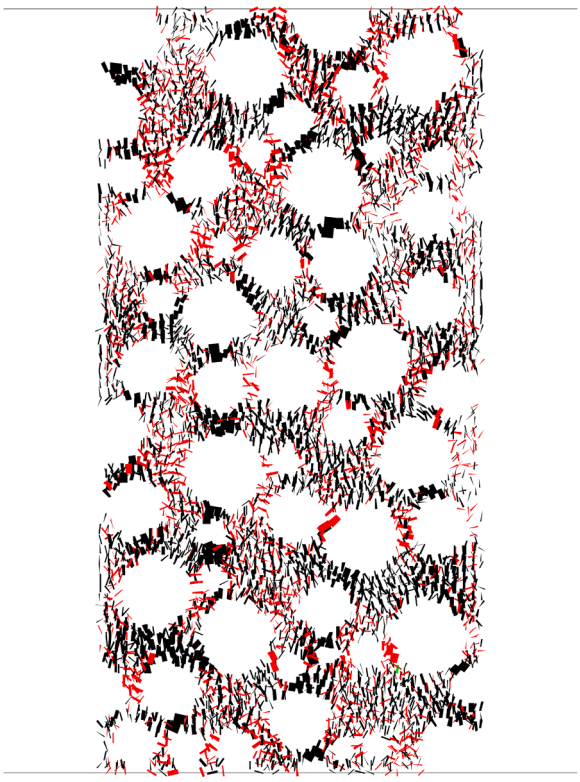

Fig. 6. Stress concentration near some clumps (black for compression and red for tension, the width of them means magnitude of stress).

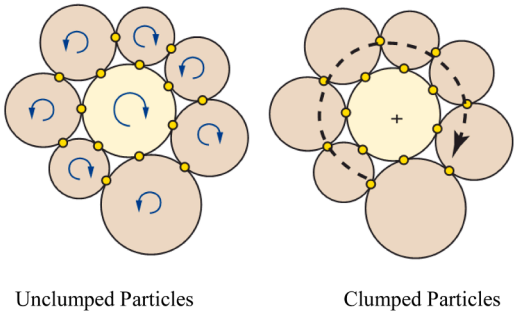

Fig. 7. Particle rotation mechanisms in unclumped and clumped particles.

The clump can suppress particles rotation and add the stiffness and strength to assemble. In partly clumped assemble, the results were given in Fig. 9 shown clearly that peak strength, crack initiation stress and elastic modulus are all significantly increased as clump's content increases.

2.3.4. *Accumulation of cracks*

Elastic mismatch causes stress concentration. Such stress is larger than average stress in sample, when the concentrated stress excesses the bond strength either particle-particle or particle-clump, breaks occur.

Fig. 10 indicates that at low axial stress level, the crack begins to accumulate in partly clumped assemble, while Fig. 11 indicates that crack begins after axial stress reaching nearly half of peak strength in unclumped assemble, and the number of cracks increase rapidly near peak strength. Such phenomenon can explain by elastic mismatch in partly clumped assemble and there is no such mismatch in unclumped assemble.

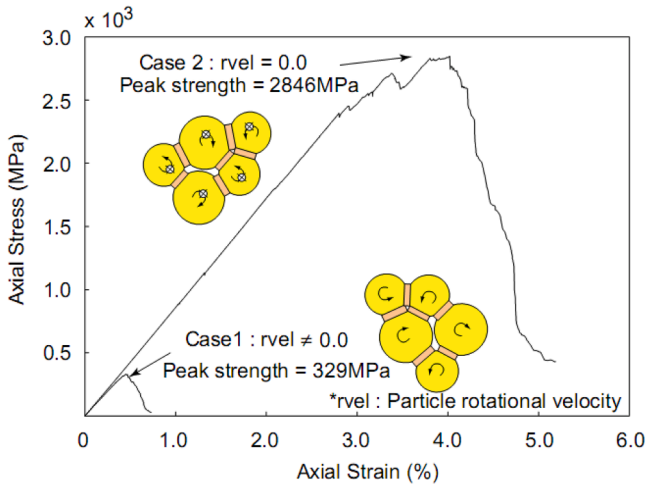

Fig. 8. Effect of particle rotation. Note that as particle rotation is completely suppresses, peak strength is increased an order of magnitude.

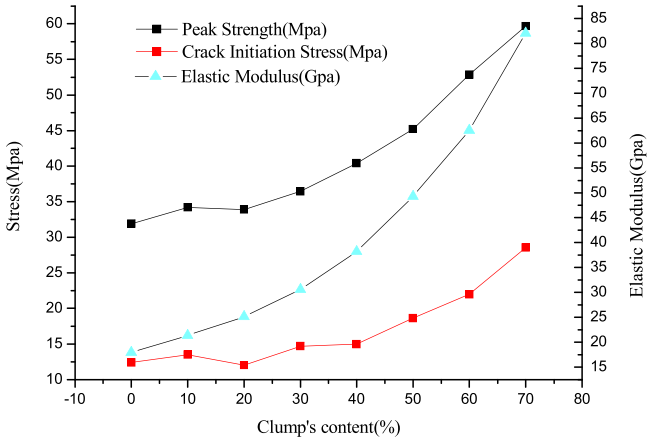

Fig. 9. Effect of clump's content on peak strength and crack initiation stress as well as elastic modulus (the radius of clump was kept 2.0 ± 1 mm for all).

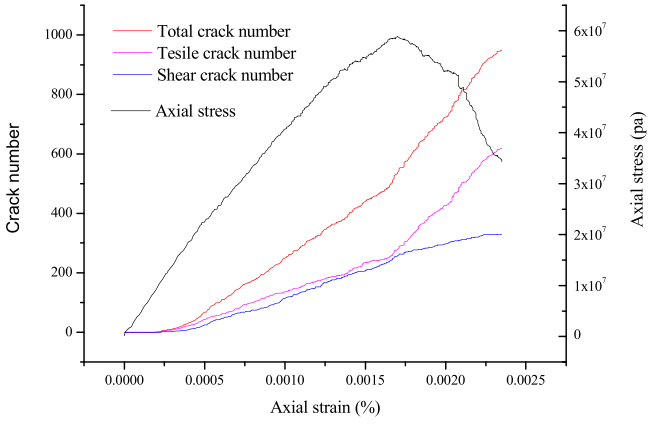

Fig. 10. Crack growth in partly clumped assemble(clump's content 50 %).

3. Joint planes model for schist

3.1. Joint planes model

Despite elastic mismatch between quartz and mica, quartz mica schist is a transverse anisotropy material with fabric which is

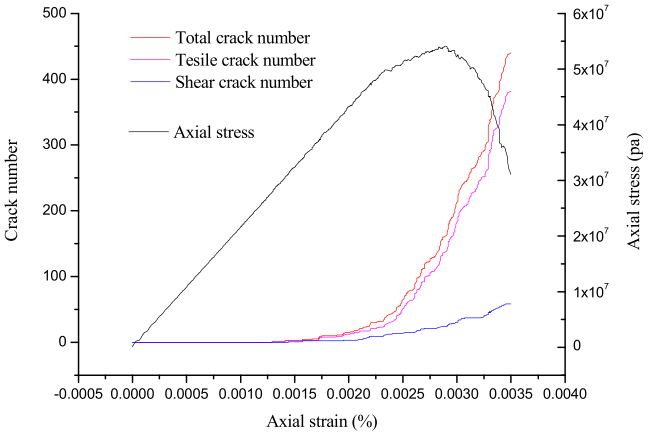

Fig. 11. Crack growth in totally unclumped assemble.

symmetrical about an axis perpendicular to the foliation [4]. In transversely isotropic rock, peak strength varies with respect to the orientation of the plane of weakness.

To gain valuable insights into the anisotropism induced by mica schist, it is essential to test joint planes with various orientations at significant stress levels and under different stress paths. However, implementing such an experimental program in a laboratory or in-situ setting is challenging due to its complex procedure, time-consuming nature, and high costs. Field investigations were shown that the joint planes densities and orientations of gneissic mica schist changed frequently for the quartz dike invasion (Fig. 12), so it would be impossible to gain a series of samples with the same configuration strictly. However, from large fields scale, the joint plane's orientations of gneissic mica schist were found to have regular arrangement. This regular arrangement has great influence on cave and slope stability. Numerical simulation can fulfill the aforementioned requirements; numerous studies have been conducted using numerical modeling with joint planes in BPM, primarily to investigate failure modes and assess how joint orientation influences the strength and deformation of gneissic mica schist.

D.Potyondy & J.Autio [27] have created two best-fit isotropic materials to bind the laboratory response set to represent the gneissic tonalite. The upper-bound material corresponds to the maximum modulus and strength (E = 80 GPa, UCS=140 MPa), while the lower-bound material corresponds to the minimum modulus and strength (E = 62 GPa, UCS=90 MPa). F.-S. Jeng and T.-T. Wang [28] employed a bonded particle model for interlayered rocks, utilizing two layers of equal thickness, where one layer is stronger and stiffer than the other. Both used two materials to simulate the weak plane and

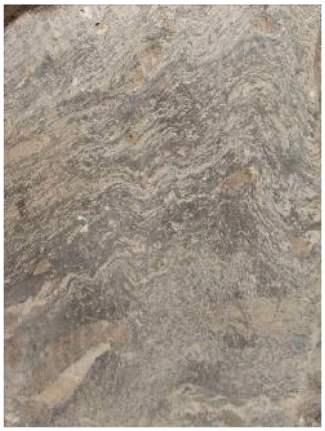

Fig. 12. Quartz dike invasion.

inter-layer. In fact, mica schist is only sorts of weak plane with no thickness, and both sides of weak plane have the same property. Therefore, another method to simulate the mica schist should be considered.

Joint planes can be defined in PFC2D to represent surfaces along which sliding and separation can occur between bonded groups (or clusters) of particles. The direction normal to each plane lies in the xy-plane; thus, the planes map into lines in a PFC2D model [16]. A joint-plane contact is defined as a contact that occurs between balls located on opposite sides of the joint plane. These joint-plane contacts can be designated with a contact model and properties that differ from those assigned to contacts not located on the plane. Such plane has met the need to simulate mica schist, and also can represent fractures, fissures, joints, faults or bedding planes in a geologic medium. This joint plane model for mica schist was taken into use.

3.2. *Effect of Joint plane's bond strength*

Parameters in Table 2 for biotite are used in this section for Joint plane effect test, a set of parallel joint planes (with the same distance *d*, d=4 mm in this parametric study) were made for mica schist (Fig. 13). All joint-plane's contacts were assigned the same properties; the properties would be changed during test in order to observe the influence of macro-properties of assemble.

As illustrated in Table 2, the mica's normal and shear bond strengths $\overline{\sigma}_c=\overline{\tau}_c=$ 30Mpa± 8Mpa, the joint plane's bond strength was assign to 0.1, 0.3, 0.6, 0.9 times of mica's bond strength and joint plane's particle friction to 0, the results are given in Fig. 14(for peak strength), Fig. 15 (for crack initiation stress), Fig. 16(for Elastic modulus) under different angles. Note that a joint plane assigned weak (e.g., low friction or bond strength) properties on the plane will not, in general, lead to sliding on the plane directly, because of the roughness of the plane [16]. The particle-friction coefficient seems to only influence the post-peak response, and as of now, it is unclear how it should be calibrated. Friction of joint plane's particles were set 0, but it does not mean the friction of joint plane is 0, however, it is the lowest value that can be given to describe smooth mica schist.

Fig. 14 shows that joint plane's bond strength affects the peak strength greatly, when joint plane's bond strength decrease (from 0.9 to 0.1 times of mica's bond strength), the peak strength decreases and the anisotropism increase which showed a U Shape under different angle as

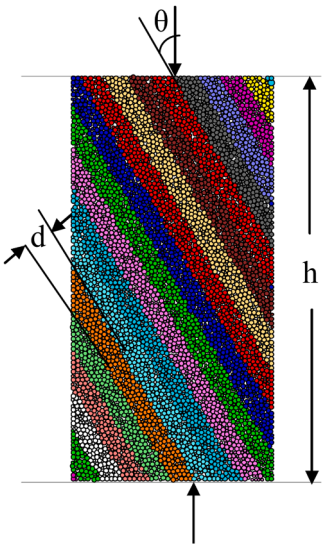

Fig. 13. Schematic illustration of the adopted joint plane model for mica schist. The interfaces between different colors are joint plane, except the joint plane, all particles have the same properties.

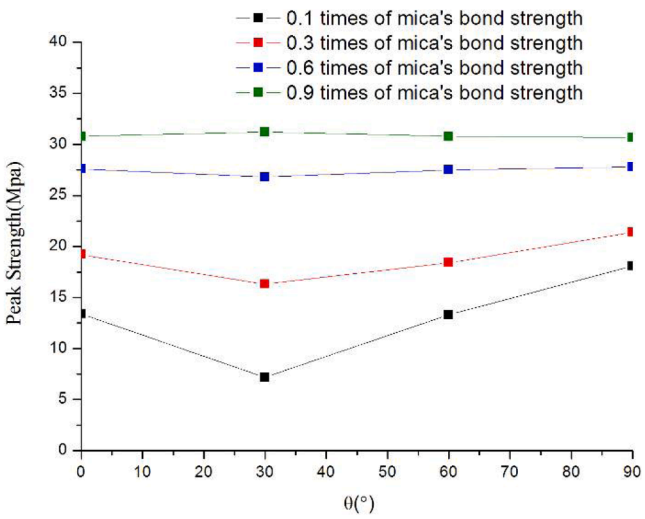

Fig. 14. Peak strength under different angle θ.

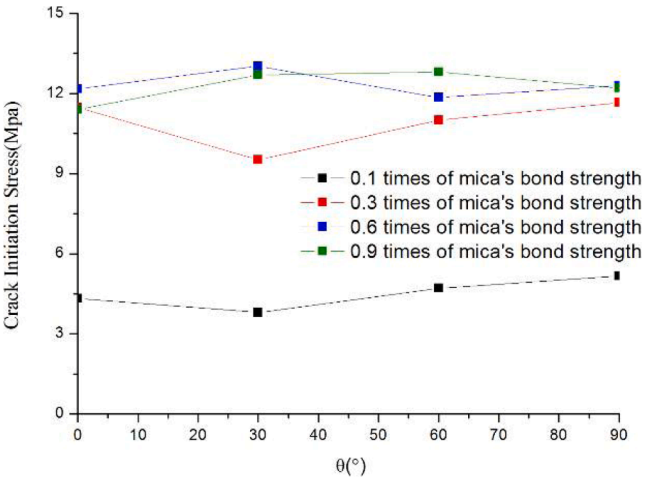

Fig. 15. Crack initiation stress under different angle θ.

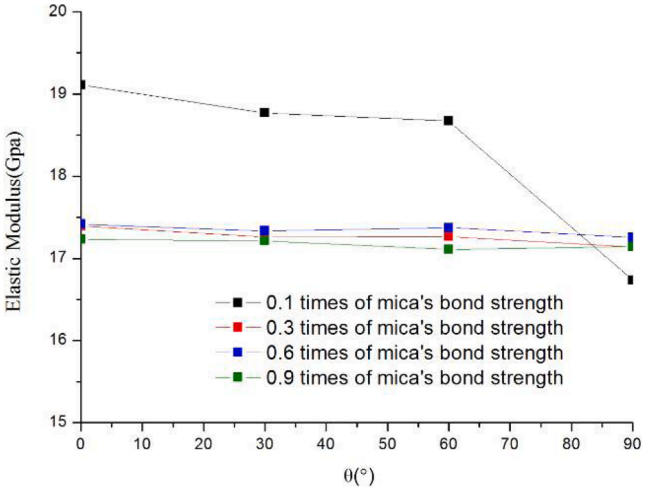

Fig. 16. Elastic modulus under different angle θ.

M.H.N. Behrestaghi [29]. Crack initiation stress (Fig. 15) shows similar rules as peak strength, except for slightly fluctuate between 0.6 and 0.9 times of mica's bond strength.

Elastic Modulus showed in Fig. 16 indicates that the elastic modulus increases for joint plane's bond strength decrease. However, the increase exhibits irregularity, which may be attributed to the Elastic Modulus being calculated using the stress and strain increments between the test's start and the point where half of the peak stress is reached. Consequently, the modulus is not solely dependent on particle parameters but also on the peak strength.

4. Calibration of PFC to DanBa quartz mica schist using partly clumped particles and joint plane model

4.1. DanBa quartz mica schist

Similar to numerous layered rock formations that have been modeled in previous researches [23,30], DanBa quartz mica schist exhibits prominent schistosity and a parallel alignment of mineral grains, which is apparent through the visible banding that does not require magnification (Fig. 17). Sorts of quartz mica schist mainly contains minerals such as mica, quartz and plagioclase (Table 4). Mica and quartz which account for more than 90 % of volume are the main parts of quartz mica schist. The quartz is harder (with larger elastic modulus and smaller Poisson's ratio) than the biotite, muscovite, plagioclase feldspar (Table 1).

4.2. Laboratory test analysis

Testing samples for determining the unaxial compressive deformational behaviour of rock are $\Phi 50 \pm 1 \times 100 \pm 2$ mm, the loading rate applied in these tests were chosen as 0.002 mm/s. Testing procedures include recording the axial (ε_{axial}) and lateral ($\varepsilon_{lateral}$) strains in a sample as it is loaded with axial stress. In 1928, Richart et al. [31] first emphasized the significance of volumetric strain, alongside axial and lateral strains, in compression testing. Cook [32] subsequently confirmed that the volumetric strain measured by surface strain gauges on a sample represents a pervasive volumetric property of the rock, rather than a superficial phenomenon. For a cylindrical sample subjected to axial loading, with or without confining stress, and under small strains, the volumetric strain is calculated as follows:

$$\varepsilon_v = \frac{\Delta V}{V} \approx \varepsilon_{axial} + 2\varepsilon_{lateral} \tag{5}$$

By plotting the axial, lateral, and calculated volumetric strains against the applied axial stress, one can trace the path of a rock sample leading to failure. Figures for DanBa quartz mica schist in uniaxial compression was given in Fig. 18 and Fig. 19.

C.D. Martin [33] has demonstrated that the stress-strain curves for brittle rocks can be divided into five regions (Fig. 18). The initial region of these curves corresponds to the closure of existing microcracks within the sample, which may or may not be present depending on the initial crack density and geometry. In the case of schist orientation perpendicular to loading direction (Fig. 18), the closure process is clear and lasted to axial strain of 0.172 %, when schist orientation was parallel to loading direction (Fig. 19), the closure process was short and just lasted to axial strain of 0.08 %. It may be explained that the existing microcracks is mainly orientated along the schist plane.

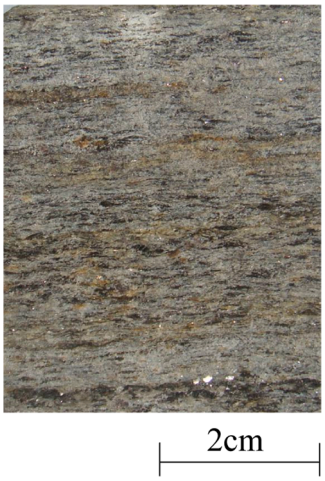

Fig. 17. clear schistocity of quartz mica schist (from Danba, Sichuan, China).

Table 4
DanBa quartz mica schist mineral contents.

mineral	mica	quartz	plagioclase	others
content	40.5	52.1	6.7	0.7

After the existing cracks have closed, the rock is presumed to behave as a linear, homogeneous, elastic material (Region II). The linear region is evident when the schist orientation is perpendicular to the loading direction (Fig. 18), whereas it appears blurred and brief when the schist orientation is parallel to the loading direction (Fig. 19). Microcracks may occur simultaneously with the closure process due to the lower tensile strength between schist layers compared to their compressive strength.

The onset of dilation starts at the beginning of Region III. Brace et al. [34] found that dilation began at a stress level of about 30–50 % of the peak strength. For sample 1 and 2, the stress levels are about 38.8 % and 32.6 % of the peak strength respectively, the value of each are 10.1Mpa and 7.1Mpa. It is important to note that this dilation is only detected by the lateral strain gauge, indicating the growth of axial cracks, i.e., cracks parallel to the direction of the maximum applied load. This stress level will be termed as the crack-initiation stress (σ_{ci}). Identifying crack initiation from laboratory stress-strain curves can be challenging, especially when the sample already contains a high density of microcracks aligned with the direction of the maximum applied load (Fig. 19). The crack-initiation stress is determined by plotting crack volumetric strain against axial strain, where it corresponds to the axial stress at which dilation first appears on the crack-volume plot.

The crack volumetric strain is calculated as follows. Initially, the elastic volumetric strains are determined using the elastic constants (E,ν) obtained from the linear portion of stress-strain curves in Region II, according to the formula:

$$\Delta V \Big/ V_{elastic} = \frac{1-2\nu}{E}\left(\sigma_1 - \sigma_3\right) \tag{6}$$

The crack volumetric strain is then determined by subtracting the elastic volumetric strains from the total volumetric strain that has been measured.

The axial stress level at which the total volumetric strain reversal occurs signifies the commencement of Region IV and indicates the initiation of unstable crack growth, as outlined by Bienawaski [35]. Typically, this occurs within an axial stress range of 70–85 % of the short-term peak strength, marking the point where the axial strain ceases to be linear. The increase in load beyond the unstable crack stress represents a temporary strain-hardening effect that cannot be depended upon for sustained loading conditions. Therefore, this stress level will be termed the crack-damage stress (σ_{cd}), as loads exceeding this threshold lead to unacceptable material damage under permanent loading.

It's interesting that when sample's schist orientation perpendicular to loading direction shown in Fig. 16, the value of σ_{cd} is 18.47Mpa, about 70 % of the short-term peak strength(26.05Mpa), while sample's schist orientation parallel to loading direction shown in Fig. 19, the value of σ_{cd} is 9.49Mpa, only 43.5 % of the short-term peak strength (21.787Mpa). It means that the crack-damage stress varies greatly for the schist orientation, the simulation of such anisotropism of the quartz mica schist will be discussed in the following pages.

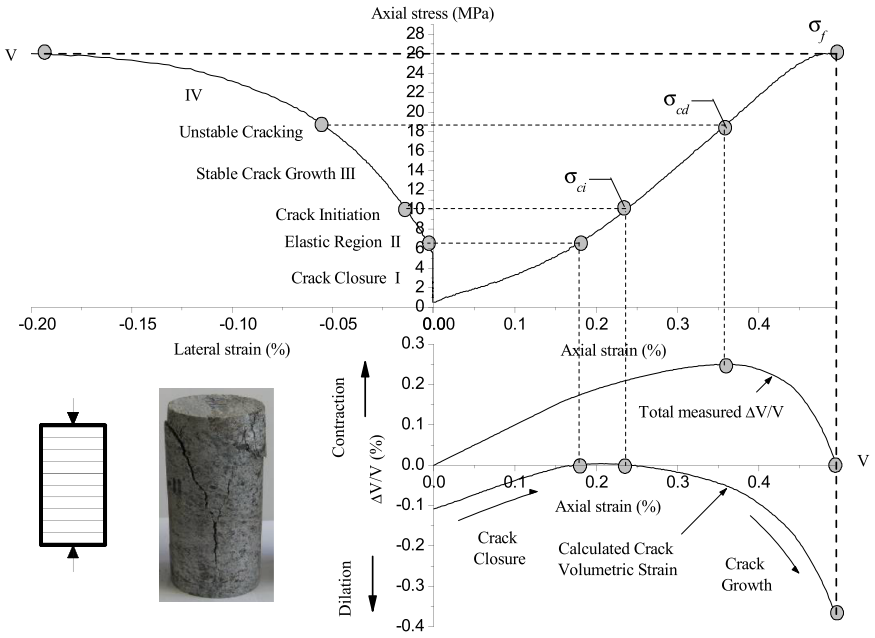

Fig. 18. Stress-strain diagram obtained from a DanBa quartz mica schist sample 1 (schist orientation perpendicular to loading direction).

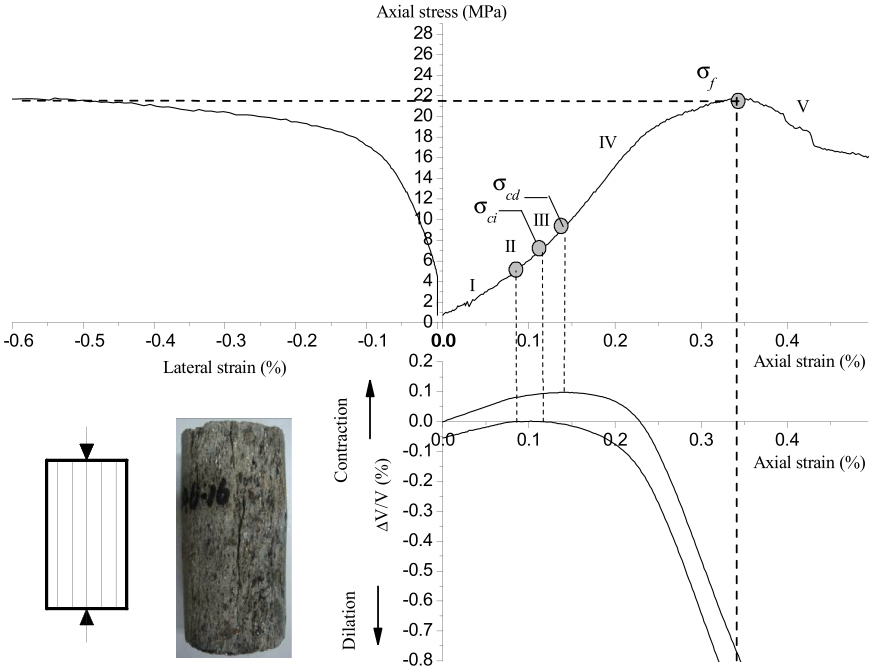

Fig. 19. Stress-strain diagram obtained from a DanBa quartz mica schist sample 2 (schist orientation parallel to loading direction).

4.3. Choosing material properties for model

While it may be straightforward to assign specific properties to a BMP model, selecting properties that closely mimic the behavior of a targeted physical material can be challenging, particularly in the context of a model that combines partly clumped particles with joint planes, as this introduces numerous additional parameters that must be considered. This section will describe how to match elastic properties, peak strength and crack-initiation stress. The following calibration sequence should be followed to minimize iterations.

(1) Match the Young's modulus by setting material strength to a large value and varying elastic modulus. Then match the Poisson's ratio by varying the particle and bond stiffness ratio (normal to shear). It may be necessary to perform some iteration to match both values, the process should be according to the rules revealed by parametric studies in Section 2 to minimize iterations.

In this partly clumped-particle combined with joint planes model, parameters have three main groups: unclumped particles, clumped particles and joint planes.

The strength parameters include: parallel bond strength of unclumped particles $\overline{\sigma}_c$ and $\overline{\tau}_c$, parallel bond strength of clumped particles clp_pb_nstr and clp_pb_sstr, joint planes strength j_pb_nstr and j_pb_sstr.

The elastic modulus parameters include: contact modulus E_c and parallel bond modulus $\overline{E}_c$ of unclumped particles, contact modulus clp_E_c and parallel bond modulus $clp\_\overline{E}_c$ of clumped particles, joint planes modulus j_kn and j_pb_kn.

Stiffness ratio parameters include: contact stiffness ratio $k_n/k_s$and parallel bond stiffness ratio $\overline{k}_n/\overline{k}_s$ of unclumped particles, contact stiffness ratio clp_kn/ clp_ks and parallel bond stiffness ratio clp_pb_kn/clp_pb_kn of clumped particles, contact stiffness ratio j_kn/s_ks and parallel bond stiffness ratio j_pb_kn/ j_pb _ks of joint planes.

(2) Once the desired elastic response has been achieved, align the peak strength at zero confinement by adjusting the mean material strength while setting the standard deviation of material strength to zero. The strength of unclumped particles, clumped particles and joint planes all affect the peak strength, during the iteration process we should keep the strength of clumped particles much larger than unclumped particles, the strength of unclumped particles larger than joint planes.

(3) Now match the crack-initiation stress by increasing the standard deviation of material strength. We just consider the standard deviation of unclumped particles and set the deviation of clumped particles as well as joint planes to zero. This step may reduce the peak strength and, thus, a few iterations between steps 2 and 3 may be required.

(4) If one desires to reproduce post-peak behavior, vary the particle friction coefficient μ, clp_μ and j_μ. In this research no attempt to match the post-peak behavior.

4.4. PFC simulation for unaxial compressive test

There exists evidence from the parametric study that introducing the partly clumped model and joint plane is more realistic and effective for modeling of quartz mica schist rock in PFC. In this section such model was applied to simulate DanBa quartz mica schist and the results were compared with unaxial compressive test described in Section 4.2.

According to Table 4, 52.1 % clumped particles stand for quartz were taken, as hard mineral, while 47.9 % unclumped particles for mica+-plagioclase+others were considered as soft mineral. The final clump size for the simulation was 0.64 ± 0.32 mm, about the grain size of quartz for DanBa quartz mica schist. All parameters are listed in Table 5 for DanBa quartz mica schist, these parameters mainly take from Table 2 and Table 3. The density of particle was set to 3210 kg/m^3, which was calculated from the density of DanBa quartz mica schist 2686 kg/m^3 for considering the spacing between particles. The elastic modulus and strength of unclumped particles for mica were reduced for considering the micro-cranny and tiny bug. Finally, the desirable sets of micro-parameters were found by "trial and error" according to the rules detected by parametric study before and calibration sequence in Section 4.3.

Fig. 20 shows the comparison of axial stress-strain and lateral strain response between PFC synthetic rock and DanBa quartz mica schist sample 1. Although PFC exhibits slightly linear, overall responses for axial stress-strain are well matched. Compared with the laboratory results, the initial non-linearity was not present because no initial flaws or pore effects were modeled in PFC, such phenomenon was also revealed by N. Cho and C.D. Martin [10] in totally clumped model. If a random distribution of pores or cracks were employed, the nonlinearity

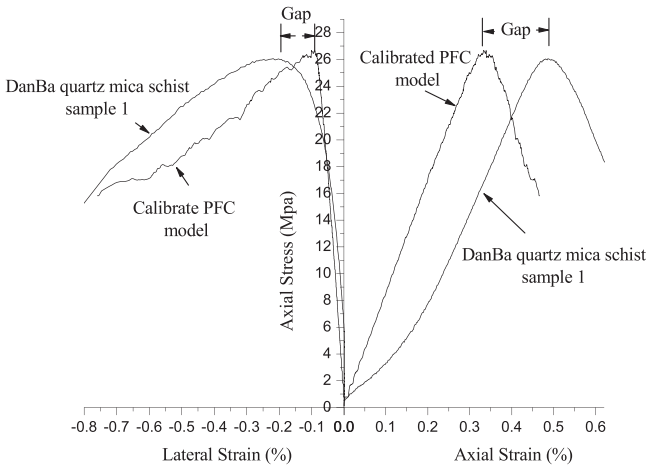

Fig. 20. Comparison of predicted axial stress-strain and lateral strain response from the calibrated PFC to the measured laboratory response of DanBa quart mica schist sample 1.

measured could potentially be captured in PFC [36–38]. However, modeling this initial pore effect lies outside the scope of our current research endeavors.

As a matter of fact, because of the lack of strain caused by the close of initial flaws or pores, there are gaps between PFC model and test sample, not only axial but also lateral strain. For the initial flaws or pores mainly arranged along the schist plane, the gap distance differs for the schist orientation. When schist orientation perpendicular to loading direction (Fig. 20), the gap distance of axial strain becomes larger than that of schist orientation parallel to loading direction (Fig. 22), while the gap distance of lateral strain is reverse.

The shape of the failure zone in PFC showed the typical macro shear fractures observed in the laboratory test of sample 1(Fig. 21), while schist orientation parallel to loading direction, the failure zone in PFC shown the mainly macro tensile fractures observed in the laboratory test of sample 2(Fig. 23).

As has been discussed in Section 2.3.2, we take crack initiation stress corresponds to approximately 2 % of total number of cracks as Potyondy and Cundall [8] suggested. The crack initiation stress of calibrated PFC sample 1 and sample 2 are illustrated in Fig. 24 and Fig. 25, 37 % $\sigma_f$and 31 % σ_f of each respectively. These two values are well matched with laboratory result (38.8 % $\sigma_f$and 32.6 % σ_f in Fig. 18 and Fig. 19).

M.S. Diederichs and P.K. Kaiser [39] used the crack density $\chi(\chi = A^{-1}\sum d^2$ *where* d is the crack length and A is the 2D PFC sample area) versus axial stress curve to determine first crack, systematic cracking and first interaction of crack. In this research the particle radius distributes between 0.25 mm and 0.415 mm, the crack length between particles will not be fluctuated very much, so we can take the crack number instead of the crack density to determine the crack damage stress. We take the point that the crack numbers start to accelerate, as is illustrated in Fig. 24 and Fig. 25, 74 % $\sigma_f$and 44 % σ_f of each respectively. These two values are also well matched with laboratory result

Table 5
Micro-parameters of DanBa quartz mica schist for calibration.

R_{min}	0.25 mm	R_{max}/R_{min}	1.66	clp_rad	0.64 ± 0.32 mm	j_dis	2 ± 0.2 mm
E_c	8.45Gpa	$\overline{E}_c$	8.45Gpa	*clp_*E_c	47.88 Gpa	*clp_*$\overline{E}_c$	47.88 Gpa
k_n/k_s	2.5	$\overline{k}_n/\overline{k}_s$	2.5	clp_kn/ clp_ks	0.6	clp_pb_kn/ clp_pb_kn	0.6
$\overline{\tau}_c$	20Mpa± 3Mpa	$\overline{\sigma}_c$	20Mpa± 3Mpa	clp_μ	0.1	clp_pb_nstr	60 ± 0Mpa
μ	0.1	$\overline{\lambda}$	1.0	clp_pb_sstr	60 ± 0Mpa	*clp_*$\overline{\lambda}$	1.0
j_kn	5Gpa	j_pb_kn	8.5e12	j_μ	0.0	j_pb_nstr	4.5 ± 0Mpa
j_kn/s_ks	2.5	j_pb_kn/j_pb _ks	2.5	j_pb_sstr	15 ± 0Mpa	*j_*$\overline{\lambda}$	1.0

Prefix "clp_" stand for parameters for clump, prefix "j_" stand for parameters for joint planes.

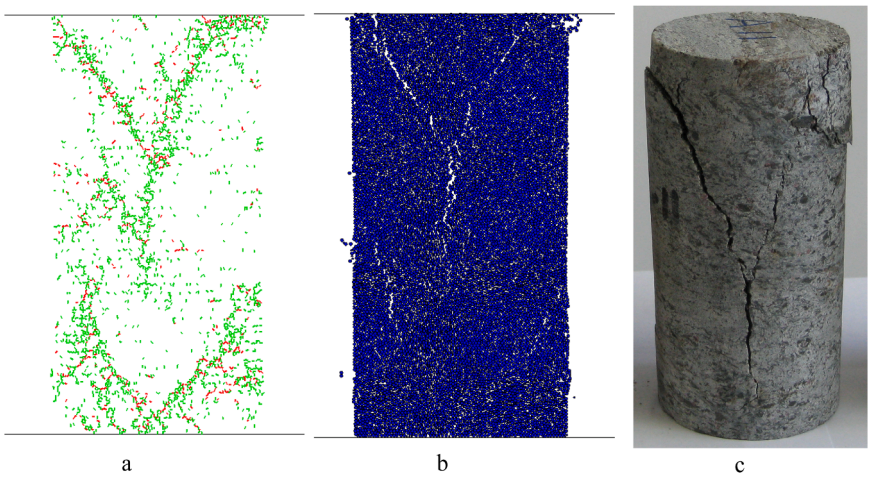

Fig. 21. Sample 1 failure in uniaxial compression test for the calibrated PFC and the observed failure in laboratory test. (a) Crack distribution, (b) sample dilation and (c) synthetic rock failure.

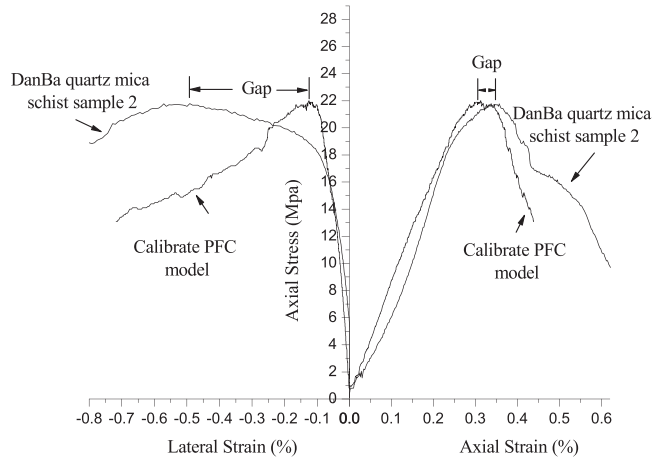

Fig. 22. Comparison of predicted axial stress-strain and lateral strain response from the calibrated PFC to the measured laboratory response of DanBa quart mica schist sample 2.

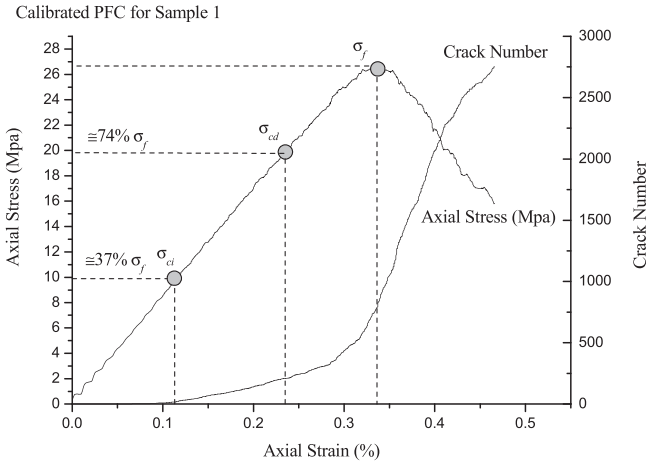

Fig. 24. Axial stress-strain and crack number-axial strain curves for calibrated PFC for sample 1.

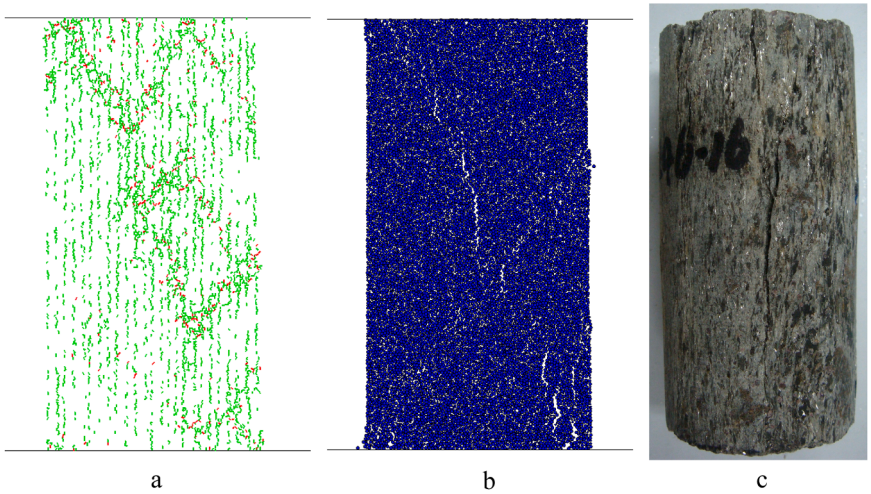

Fig. 23. Sample 2 failure in uniaxial compression test for the calibrated PFC and the observed failure in laboratory test. (a) Crack distribution, (b) sample dilation and (c) synthetic rock failure.

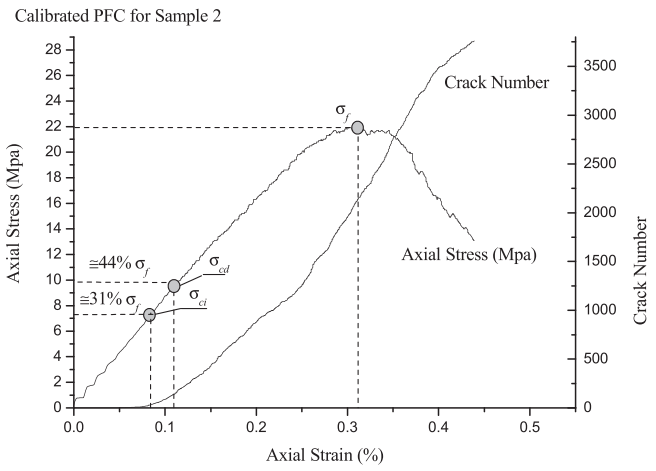

Fig. 25. Axial stress-strain and crack number-axial strain curves for calibrated PFC for sample 2.

(70 % $\sigma_f$and 43.5 % $\sigma_f$in Fig. 18 and Fig. 19).

Microcracks first generate around the hard minerals (Fig. 26) and along the joint planes (Fig. 27), the cracks orientation parallel to the loading direction and mainly tensile crack at initial stage. This phenomenon just fit the stress concentration around hard mineral caused by elastic mismatch and the joint plane's particle strength is weaker than others.

5. Conclusion

The bonded particle model has been widely used to model brittle failure. Many macroscopic rock peculiarities can be simulated by using a series of micro parameters and interaction law for disks bond contacts. Partly clumped-particles for elastic mismatch of minerals and joint planes for schist were adopted to describe the DanBa quartz mica schist.

Elastic mismatch between grains causing stress concentration was simulated by partly clumped assemble. The modulus of biotite as soft mineral, quartz as hard mineral was used for parametric studies. The results showed that the intensity of stress concentration and elastic modulus was significantly increased as clump size increased, however,

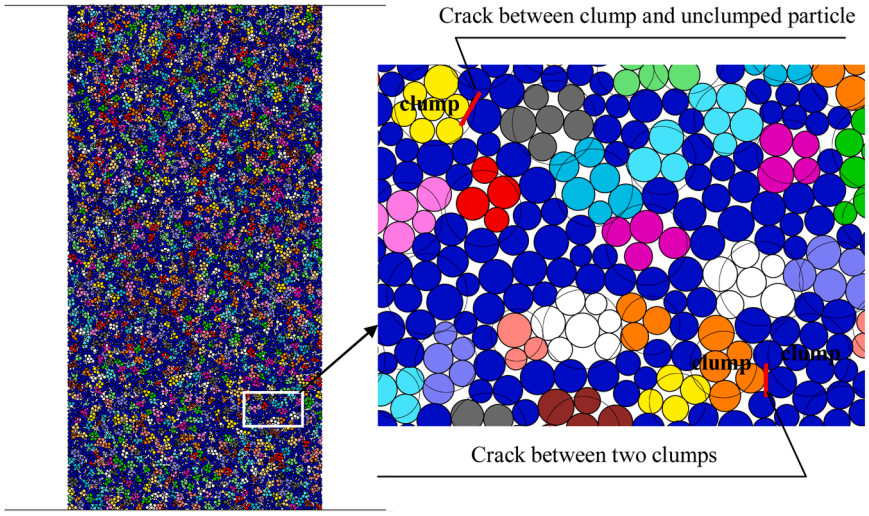

Fig. 26. Crack in PFC calibrated sample 1 at crack initiation (loading stress 9.835Mpa≈37 %σ_f), show in clump form.

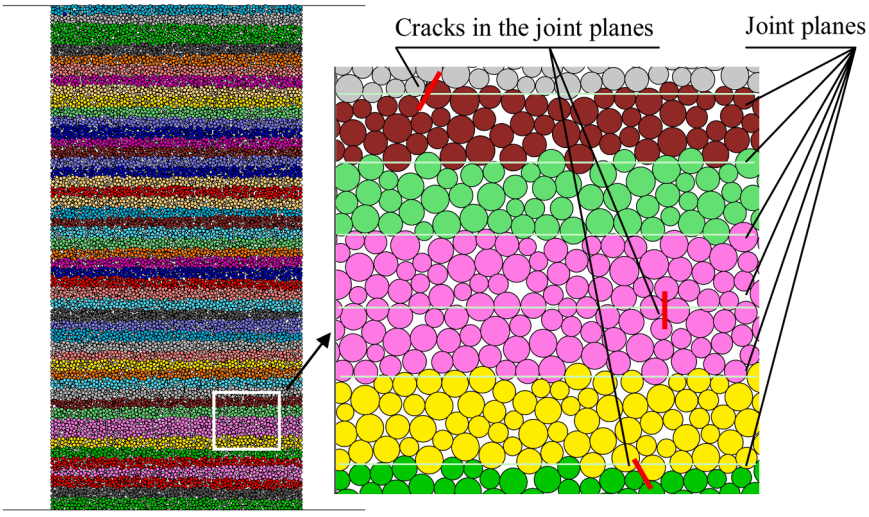

Fig. 27. Crack in PFC calibrated sample 1 at crack initiation (loading stress 9.835Mpa≈37 %σ_f) show in joint plane(schist) form.

the crack initiation stress as well as peak strength reduced as clump size increased; crack initiation stress, peak strength and elastic modulus were all significantly increased as clump's content increased.

Joint plane was adopted for mica schist, test results showed that joint plane's bond strength affected the peak strength greatly, when joint plane's bond strength decreased, the peak strength decreased but the anisotropism increased and showed the U Shape under different angles, crack initiation stress showed similar rules as peak strength.

Partly clumped-particles combined with joint planes model was used to simulate the anisotropic of DanBa quartz mica schist, and the results were well matched with uniaxial compressive test. Currently, the calibration between DanBa quartz mica schist and PFC was made by using the uniaxial compressive test. More complex loading paths need to be evaluated to investigate whether the same agreement as observed in this study can be achieved using PFC to model triaxial test and engineering problems such as rock slopes and tunnels.

CRediT authorship contribution statement

Wu Shunchuan: Methodology. **Wang Sijing:** Supervision. **Zhang Xiao-Ping:** Writing – review & editing, Writing – original draft, Investigation, Funding acquisition.

Declaration of Competing Interest

The authors declare that they have no known competing financial interests or personal relationships that could have appeared to influence the work reported in this paper.

Acknowledgments

This work has been supported by the Natural Science Foundation of Hubei Province (2021CFA081) , the Fundamental Research Funds for the Central Universities (2042023kf0210) and the National Natural Science Foundation of China (42277160). Many thanks are given to Dr. Cho N, Dr. Lan H. X. for kind helps.

References

[1] Arup K. Khaund, Patrick S. Nicholson, Fracture of a brittle composite: influence of elastic mismatch and interfacial bonding, J. Mater. Sci. 15 (1) (1980) 177–187.
[2] Kee Sung Lee, Effect of elastic modulus mismatch on the contact crack initiation in hard ceramic coating layer, J. Mech. Sci. Technol. 17 (12) (2003) 1928–1937.
[3] P.D. Warren, D.A. Hills, The influence of elastic mismatch between indenter and substrate on Hertzian fracture, J. Mater. Sci. 29 (11) (1994) 2860–2866.
[4] J.A. Hudson, J.P. Harrison, Engineering Rock Mechanics. Part I: An Introduction to the Principles, Pergamon, Amsterdam, 1997.
[5] D. Ellis, J. Howard, et al., Mineral logging parameters: nuclear and acoustic, Tech. Rev. 36 (1) (1988) 38–55.
[6] A.F. Woeber, S. Katz, et al., Elasticity of selected rocks and minerals, Geophys 28 (1963) 658–663.
[7] Gary Mavko, Tapan Mukerji, et al., The Rock Physics Handbook, Cambridge University Press, Cambridge, 2003.
[8] D.O. Potyondy, P.A. Cundall, A bonded-particle model for rock, Int. J. Rock. Mech. Min. Sci. 41 (2004) 1329–1364.
[9] A. Fakhimi, Application of slightly overlapped circular particles assembly in numerical simulation of rocks with high friction angles, Eng. Geol. 74 (2004) 129–138.
[10] N. Cho, C.D. Martin, D.C. Sego, A clumped particle model for rock, Int. J. Rock. Mech. Min. Sci. 44 (2007) 997–1010.
[11] J.M. Kemeny, N.G.W. Cook, Micromechanics of deformation in rocks, Kluwer Academic Publishers, Dordrecht, 1991.
[12] R.W. Lounsbery, T.R. West, Petrography of some Indiana aggregates in relation to their engineering properties, Univ. Ky. Eng. Exp. Station Bull. Ser. 20 (2) (1965) 24–41.
[13] Lundquist, S. and M. Göransson. Evaluation and interpretation of microscopic parameters vs. mechanical properties of Precambrian rocks from the Stockholm region, Sweden. Proceeding of the 8th Euroseminar on Microscopy Applied to Building Materials, Athe`nes departement de géologie,. Athens 2001; 13-20.
[14] D.E. Moore, D.A. Lockner, The role of microcracking in shear-fracture propagation in granite, J. Struct. Geol. 17 (1995) 95–114.
[15] Hengxing Lan, C.Derek Martin, Bo Hu, Effect of heterogeneity of brittle rock on micromechanical extensile behavior during compression loading, J. Geophys. Res. 115 (2010) B01202.
[16] PFC2D (Particle Flow Code in 2 Dimension) Version 3.1. Minneapolis: Itasca Cons Group2004.
[17] Zhang Xiao-Ping, Wong Louis Ngai Yuen, Loading rate effects on cracking behavior of flaw-contained specimens under uniaxial compression, Int. J. Fract. 180 (1) (2013) 93–110.
[18] Zhang Xiao-Ping, Wong Louis Ngai Yuen, Choosing a proper loading rate for bonded-particle model of intact rock, Int. J. Fract. 189 (2) (2014) 163–179.
[19] Zhang Qi, Zhang Xiao-ping*, A numerical study on cracking processes in limestone by the b-value analysis of acoustic emissions, Comput. Geotech. 92 (2017) 1–10.
[20] Zhang Xiao-Ping, Zhang Qi, Wu Shunchuan, Acoustic emission characteristics of the rock-like material containing a single flaw under different compressive loading rates, Comput. Geotech. 83 (2017) 83–97.
[21] Zhang Qi, Zhang Xiao-Ping*, Yang Sheng-Qi, A numerical study of acoustic emission characteristics of sandstone specimen containing a hole-like flaw under uniaxial compression, Eng. Fract. Mech. 242 (2021).
[22] M.S. Diederichs. Instability of hard rock masses: the role of tensile damage and relaxation, University of Waterloo. PhD, 2000.
[23] P.-Z. Pan, F. Tan, F. Li, F. Chi, X. Liu, Z. Wang, A three-dimensional numerical study on the stability of layered rock spillway tunnels in alpine canyon areas, Deep Resour. Eng. 1 (2024) 100023.
[24] C.D. Martin, N.A. Chandler, Stress heterogeneity and geological structures, Int. J. Rock. Mech. Min. Sci. 30 (1993) 993–999.
[25] Zhang Xiao-Ping, Lv Gen-Gen, Liu Quan-Sheng, Wu Shun-Chuan, Zhang Qi, Ji Pei-Qi, Tang Xu-Hai, Identifying accurate crack initiation and propagation thresholds in siliceous siltstone and limestone, Rock. Mech. Rock. Eng. 54 (2021) 973–980.
[26] Zhang Xiao-Ping, Wong Louis Ngai Yuen, Wang Si-Jing, Han Geng-You, Engineering properties of quartz mica schist, Eng. Geol. 121 (3-4) (2011) 135–149.
[27] Potyondy D., Autio J. Bonded-particle simulations of the in situ failure test at Olkiluoto. in: Elsworth D., Tinucci J., Heasley K., editors. Rock mechanics in the national interest, Proceedings of the 38th US Rock Mechanics Symposium, 2001, pp. 1553–1560.
[28] F.-S. Jeng, T.-T. Wang, H.H. Li, T.-H. Huang, Influences of microscopic factors on macroscopic strength and stiffness of inter-layered rocks–revealed by a bonded particle model, J. Mech. 24 (4) (2008) 379–389.
[29] M.H.N. Behrestaghi, K. Seshagiri Rao, T. Ramamurthy, Engineering geological and geotechnical responses of schistose rocks from dam project areas in India, Eng. Geol. 44 (1996) 183–201.
[30] F. Tian, Z. Liu, H. Li, E. Zhang, J. Zhou, J.-f Shao, Advances in peridynamics modeling of deformation and fracturing of brittle geomaterials, Deep Resour. Eng. 1 (2024) 100110.
[31] Richart F.E., Brandtzaeg A. and Brown R.L. A study of the failure of concrete under combined compressive stresses. Bulletin no. 185. University of lllinois Engineering Experiment Station, 1928.
[32] N.G.W. Cook, An experiment proving that dilatancy is a pervasive volumetric property of brittle rocks loaded to failure, Rock. Mech. Rock. Eng. 2 (1970) 181–188.
[33] C.D. Martin, N.A. Chandler, The progressive fracture of Lac Du Bonnet granite, Int. J. Rock. Mech. Min. Sci. Geomech. Abstr. 31 (6) (1994) 643–659.
[34] W.F. Brace, B.W. Paulding Jr., C. Scholz, Dilatancy in the fracture of crystalline rocks, J. Geophys. 71 (1966) 3939–3953 (Res.).
[35] Z.T. Bieniawski, Mechanism of brittle fracture of rock, parts I, II and III, Int. J. Rock. Mech. Min. Sci. Geomech. Abstr. 4 (1967) 395–430.
[36] X.P. Zhang, P.Q. Ji, J. Peng, S.C. Wu, Q. Zhang, A grain-based model considering pre-existing cracks for modelling mechanical properties of crystalline rock, Comput. Geotech. 127 (2020) 103776, 31.
[37] Ji Pei-Qi, Xiao-Ping Zhang, Qi Zhang, A new method to model the non-linear crack closure behavior of rocks under uniaxial compression, Int. J. Rock. Mech. Min. Sci. 122 (2018) 171–183.
[38] Zhang Xiao-Ping, Zhang Pei-Yuan, Ji Pei-Qi, Zhang Han, Zhang Qi, The applicability of Brazilian test loading with different platens to measure tensile strength of rock: a numerical study, Rock. Mech. Rock. Eng. (2023), https://doi.org/10.1007/s00603-023-03566.
[39] M.S. Diederichs, P.K. Kaiser, E. Eberhardt, Damage initiation and propagation in hard rock during tunnelling and the influence of near-face stress rotation, Int. J. Rock. Mech. Min. Sci. 41 (2004) 785–812.

Professor Xiao-Ping Zhang obtained his PhD from the Institute of Geology and Geophysics, Chinese Academy of Sciences (CAS), in 2010. In 2013, he was appointed Associate Professor at the same institution. Between 2010 and 2014, he served as a Research Fellow at Nanyang Technological University in Singapore. In 2015, he joined Wuhan University as a Professor. Since 2023, he has held the position of Vice Chairman of the Tunnel Boring Machine Application Branch Council of the Chinese Society for Rock Mechanics and Engineering. His research focuses on rock mechanics for TBM excavation, and he has authored over 100 technical papers. Professor Zhang has been recognized with the Scott Sloan Best Paper Award for 2020 and the Elsevier "Tunneling and Underground Space Technology" Best Paper Award for 2023. He has been listed in Elsevier Data Repository's World's Top 2 % Scientists for both the 2022, 2023, and 2024 Single-year impact and Career-long impact (1960–2022).